analytical chemistry

Article

Cite This: *Anal. Chem.* 2020, 92, 1818−1825

pubs.acs.org/ac

Cooperation Mode of Outer Surface and Inner Space of Nanochannel: Separation-Detection System Based on Integrated Nanochannel Electrode for Rapid and Facile Detection of *Salmonella*

Wenyue Zhu,[†] Yin Chen,[†] Yawen He,[†] Weihuan Fang,[‡] Yibin Ying,[†,§] Yanbin Li,[∥] and Yingchun Fu*[,†]

[†]College of Biosystems Engineering and Food Science, Zhejiang University, Hangzhou 310058, China

[‡]College of Animal Sciences, Zhejiang University, Hangzhou 310058, China

[§]Zhejiang A&F University, Hangzhou, Zhejiang 311300, China

[∥]Department of Biological and Agricultural Engineering, University of Arkansas, Fayetteville, Arkansas 72701, United States

ABSTRACT: Nanochannels hold great prospects in intelligent systems; however, current research focuses on the inner space of the nanochannel while the outer surface is rarely explored. Here, we report on a cooperation mode of the outer surface and inner space of the nanochannel using an integrated nanochannel-electrode (INCE) and its application as a separation−detection system for rapid and facile detection of foodborne bacteria. Unlike conventional nanochannel systems, the INCE integrates two electrodes as a sensitive electrochemical interface and the nanochannel itself as nanofilter, generating a novel separation−detection system. The system is examined in a biosensing strategy based on magnetic nanoparticles (MNPs). *Salmonella typhimurium* (*St*) is taken as the target due to its severe threat to human health and food safety. By electrochemically probing the MNPs−*St* complex themselves on the surface of INCE, this method eliminates the requirement on additional signal labels. The biosensor presents a linear detection range from 10^2 to 10^7 CFU mL^{-1} and a limit of detection of 50 CFU mL^{-1}, being comparable or even better than those of analogues with complicated signal amplification designs. Moreover, the biosensor exhibits good specificity against four types of interfering bacteria. This concept may bring new insight into the development of nanochannel research and contribute a new way to the fields of separation and detection.

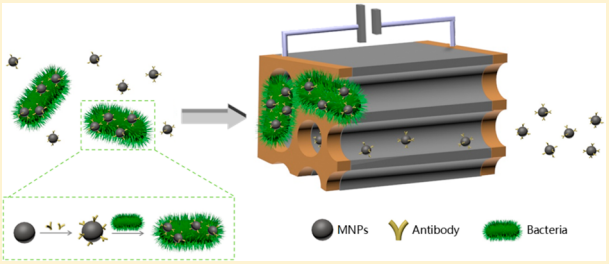

Inspired by intelligent biological ion channels in living systems, smart solid-state nanochannels have drawn ever-increasing interest recently.[1,2] Unlike fragile biological ion channels, artificial solid-state nanochannels possess mechanical and chemical stability, controllable channel shape, and tailorable surface properties. These merits benefit them with significant prospects in a wide range of fields, such as molecular filtration,[3−5] energy conversion,[6−9] and biosensors.[10−16] To date, researchers are mostly interested in the nanochannels themselves due to their smart functions including ionic selectivity, gating, and rectification.[17−20] Usually, the inner wall and space of nanochannels are engineered in order to improve the possibilities to change the surficial properties and effective diameter of nanochannels.[21−23] For instance, the inner wall of a single conical polyethylene terephthalate nanochannel was modified with *o*-phenylenediamine and rhodamine (R-110), exhibiting NO-responsive ion transport properties.[24] However, compared with the flourishing of research focused on the inner space of nanochannels, the exploration of the outer surface has been long ignored. As two close parts of nanochannels, the outer surface and the inner wall/space have great potential to be integrated to innovate strategies, such as a cooperation mode. It should open a new window to the nanochannel research and be beneficial to explore new applications.[25,26] However, the poor surface property of conventional nanochannels restricts the possibility. Therefore, to make an essential breakthrough to the surface, the appropriate surface-modification and the introduction of relevant surface-based technology are of high importance and interest.

Magnetic nanoparticles (MNPs) have been developed for widespread applications, such as separation/purification, biosensing, medicine, and drug delivery,[27−31] due to their extraordinary properties of magnetism, surface area, surficial properties, and biocompatibility.[32,33] As a commonly used tool for analytical applications, MNPs are generally modified with recognition elements such as aptamers, antibodies, and peptides for the purpose of separating and concentrating a target, minimizing interference from samples, and improving the sensitivity of the following detection.[34] However, after the collection of targets, the free MNPs without the conjugation of targets are still present in solution and unavoidably bring

Received: August 9, 2019
Accepted: November 18, 2019
Published: November 18, 2019

DOI: 10.1021/acs.analchem.9b03644
Anal. Chem. 2020, 92, 1818−1825

serious interference to the detection. More importantly, in order to generate a detection signal, current methods strongly rely on additional signal labels, such as enzymes and other types of nanomaterials.[35,36] Unavoidably, this makes the detection much more complicated, as well as brings additional procedures, costs, and operation time. Thus, the exclusion of the requirement on additional signal labels is a key but challenging issue in MNP-based analytical applications. Alternatively, the exploration of MNP−target complex itself to generate signal might be ingenious to avoid the above limitations. It should be significantly beneficial for rapid and facile detection.

Herein, a novel separation−detection cooperative system based on integrated nanochannel electrode (INCE) is developed for the rapid detection of *Salmonella typhimurium* (*St*), which is one of the most harmful food-borne pathogenic bacteria causing life-threatening diseases. Anodic aluminum oxide (AAO) nanochannel chip is adopted. To realize the concept, a new type of INCE is designed and fabricated by introducing gold layers onto both sides of an AAO nanochannel chip, as shown in Scheme 1. By exploring gold layers as electrodes, electrochemistry, a very sensitive technology to the surface property, is thus applicable and introduced to the outer surface of the AAO nanochannel array. Therefore, this method explores the outer surface of the nanochannel as electrode with high sensitivity to surface properties and the nanochannel itself as nanofilter and electrochemical cell. For the detection of bacteria, as shown in Scheme 1, MNPs modified with antibodies (MNP-Ab) are used to capture *St* (MNP-Ab-*St*), which guarantees the specificity and efficiency. After magnetic separation, the mixtures of free MNP-Ab and MNP-Ab-*St* are transferred to the surface of the INCE. Under pressure, free MNP-Ab, with size much less than the pore size of the nanochannel, penetrates through the nanochannel and is thus removed, while the MNP-Ab-*St*, with larger size than the pore, is maintained on the surface of the INCE. Finally, electrochemical impedance spectroscopy (EIS) is adopted to obtain a signal based on the hindrance of electron transfer on the INCE by MNP-Ab-*St*. This system achieves the separation−detection integration, by combining the high sensitivity of surface electrochemistry based on nanoporous electrode and high efficiency of separation based on nanochannel chip, realizing label-free, facile, and rapid separation and detection of bacteria. This concept may bring new insight into the development of nanochannel research by introducing the exploration of the outer surface of the nanochannel and contribute a new way to the fields of separation and detection, especially for those facing complicated samples but requiring rapidity and sensitivity for quantification, such as point-of-care diagnosis, food safety, and environmental monitoring.

Scheme 1. Illustration of INCE Based Separation-Detection System for the Detection of Bacteria

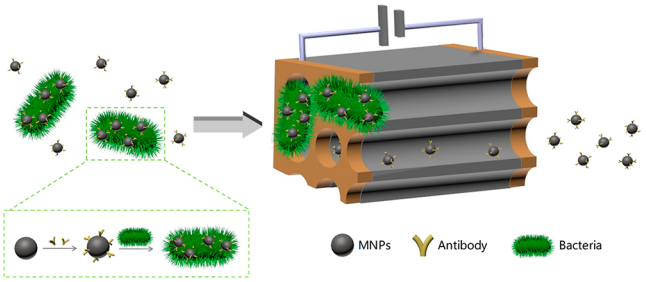

EXPERIMENTAL SECTION

Materials. All of the reagents were of analytical grade and used as received otherwise specified notification. Potassium ferricyanide ($K_3[Fe(CN)_6]$), potassium ferrocyanide ($K_4[Fe(CN)_6]$), bovine serum albumin (BSA), and 2-(*N*-morpholino)ethanesulfonic acid (MES) were purchased from Sangon Biotech Co., Ltd. (Shanghai, China). *N*-(3-(Dimethylamino)propyl)-*N*-ethylcarbodiimide (EDC) and *N*-hydroxy-sulfo succinimide sodium salt (NHSS) were purchased from Sigma-Aldrich (St. Louis, MO, USA). Brain heart infusion (BHI) and xyloselysine-tergitol 4 (XLT4) agar base were purchased from Becton, Dickinson and Company (Franklin Lakes, NJ, USA). *Salmonella typhimurium* (ATCC 14028), *Escherichia coli* O157:H7 (*Ec*, ATCC 43888), *Vibrio parahemolyticus* (*Vp*, KP9), *Listeria monocytogenes* (*Lm*, EGDe), and *Staphylococcus aureus* (*Sa*, ATCC 25923) were purchased from American Type Culture Collection (ATCC, Manassas, VA, USA). Anti-*Salmonella typhimurium* LPS antibody (Anti-*St*) was provided by Abcam (Cambridge, MA, USA). AAO nanochannel (60 μm in thickness, 4 mm in diameter, and 500 nm in pore size, parameters are provided by supplier) was purchased from Puyuan Nano (Hefei, China). Phosphate buffered saline (10 mM, pH = 7.4, 136.8 mmol·L^{-1} NaCl, 2.7 mmol·L^{-1} KCl, 10.1 mmol·L^{-1} Na_2HPO_4, 1.5 mmol·L^{-1} KH_2PO_4) was used. PBST (PBS with Tween-20) was obtained by adding 0.01% Tween-20 to PBS. MEST (MES with Tween-20) buffer (25 mM, pH = 6) was obtained through dispersing 2.6656 mg of MES powder in 500 mL of deionized water and adding 0.01% Tween-20. Borate saline buffer (BS) (200 mM, 50 mmol·L^{-1} $Na_2B_4O_7$, 200 mmol·L^{-1} H_3BO_3) was used. BST (10 mM, pH = 7.4) was obtained by diluting BS buffer by 20-fold and adding 0.01% Tween-20. Ultrapure water (Millipore, ≥18 MΩ cm) was used in all experiments. All experiments were carried out at room temperature (25 °C).

Instrumentation. All electrochemical experiments were conducted on a CHI 660E electrochemical workstation (CH Instrument Co., Shanghai, China). For a three-electrode system, one side of the INCE or Au rod electrode (φ = 2.0 mm, purchased from Tianjin Incole Union Technology Co., Ltd., Tianjin, China) served as working electrode; saturated calomel electrode (SCE) and carbon rod served as reference and counter electrode, respectively. For a two-electrode system, one side of INCE served as working electrode while the other side served as both reference and counter electrode.

The SMS0204 magnetic separator was provided by Aibit Biotech Instrument (Jiangyin, China). Scanning electron microscopic (SEM) images were collected on a GeminiSEM 300 field emission scanning electron microscope (Zeiss, Germany). Energy-dispersive X-ray spectroscopy (EDS) was conducted on an XFlash 6 | 30 Detector (BRUKER, Germany). Transmission electron microscopy (TEM) images were obtained via a JEOL JEM-1200EX transmission electron microscope (Hitachi, Japan). Dynamic light scattering (DLS) was performed on Zetasizer Nano-ZS equipment (Malvern Instruments Ltd., UK). Optical microscopy images were collected by using a H600L upright motorized microscope (*Nikon*, Japan). A Q150R ES rotary pumped dual sputtering and evaporation system (Quorum Technologies Ltd., UK) was used to sputter gold on an AAO nanochannel chip.

DOI: 10.1021/acs.analchem.9b03644
Anal. Chem. 2020, 92, 1818−1825

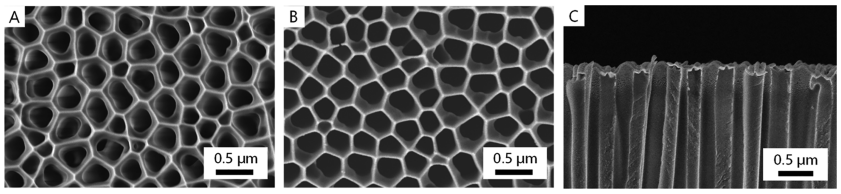

Figure 1. SEM images of the the outer surface of the pristine AAO nanochannel (A), the outer surface (B) and corresponding cross-section (C) of the INCE.

Fabrication and Modification of INCE. The fabrication process of INCE is as follows. At first, both sides of AAO were sprayed with gold (AAO-Au). The parameters of the ion sputtering were set to sputter current of 20 mA and sputter time of 400 s. Subsequently, each side of the AAO-Au chip was connected with a string of wire, and adhesive tape was then used to seal the AAO-Au chip and the wires, leaving a part of AAO-Au area on each side (φ = 1.5 mm) exposed to serve as electrodes.

The obtained INCE was cleaned in 0.5 M H_2SO_4 for about 15 min so as to remove any contaminants, followed by washing with H_2O thoroughly to remove residual H_2SO_4. Then, the clean INCE was immerged in 1 mg mL^{-1} BSA in PBS for 1 h to block the surface of electrode and nanochannel.

For a three-electrode system, cyclic voltammetry (CV) was recorded with a sweep rate of 100 mV s^{-1} from −0.1 to +0.5 V. For a two-electrode system, CV was recorded with a sweep rate of 100 mV s^{-1} from −0.4 to +0.4 V. In addition, EIS was conducted in the frequency range from 0.1 Hz to 10^5 Hz with amplitude of 5 mV.

Preparation of MNP-Ab. Carboxylic group-modified MNPs were prepared according to the reported method.[37] After washing with MEST for three times by centrifugation (10 min, 12 000 rpm, same as below), MNPs were resuspended in MEST buffer containing 10 mM EDC and 15 mM NHSS and incubated for 30 min at room temperature to activate the carboxyl group. After washing with BST for three times, the activated MNPs were resuspended in BST containing 17 μg mL^{-1} Anti-*St* and incubated for 2.5 h at room temperature. After washing, the antibody-modified MNPs were incubated with 20 mg mL^{-1} BSA in PBST for 1 h to block residual reaction sites. After washing with PBST three times, the final MNP-Ab was dispersed in PBST. When not in use, the MNP-Ab was stored at 4 °C.

Bacteria Culture and Plate Counting. The stock culture of *St* was grown in BHI broth at 37 °C overnight.[38] A series of 10-fold dilutions of the overnight cultures were made with PBS for further use. After incubating in XLT4 agar base at 37 °C for 24 h, the concentration of bacteria was determined using a plate culture method according to previous works.[39,40] Aiming at thorough sterilization, the prepared bacteria were killed in boiling water for 10 min.[41] Then, the cultures containing bacteria were centrifuged at 6000 rpm for 5 min and then dispersed in sterile PBS. The above processes were all conducted in a biosafety level 2 laboratory.

Filtration-Detection Device Incorporated with INCE. A filtration-detection device was fabricated using the 3D printing technique. It consists of two of the same pieces. Each piece contains a cylindrical channel for the flow of solution and an O-shaped groove placing a rubber O-ring. INCE was sandwiched by two pieces with the O-ring in the middle of the device. Note that the diameter of the O-ring is 4 mm larger than that of the INCE chip to avoid possible crush of INCE. For the filtration, after the injection of 10 μL solution (for example, PBST, MNP-Ab suspension or MNP-Ab-St suspension) onto one side of cylindrical channel, solution was pumped to flow through the nanochannel of the INCE to the other side (20 μL min^{-1}). For the detection, 10 μL of $K_3[Fe(CN)_6]/K_4[Fe(CN)_6]$ solution was injected into both cylindrical channels, and CV and EIS were conducted for characterization and detection.

Electrochemical Detection of Bacteria. To capture and concentrate *St* from samples, 100 μL of MNP-Ab was mixed with 1 mL of bacteria solution (from 10^2 to 10^7 CFU mL^{-1}) and incubated for 45 min at room temperature (MNP-Ab-*St*). Then the reaction solution was magnetically separated in a magnetic separator, the supernatant was discarded, and 200 μL of PBST was added. After three rounds of above washing, the final precipitates were suspended in 50 μL of PBST.

For the detection, 10 μL of the above suspension was adopted to collect EIS curves according to the procedures in section the Filtration-detection device incorporated with INCE. The suspension of MNP-Ab was used as control. The signal was set as the difference between the electron transfer resistances (R_{ct}) of the EIS results of the bacteria samples and the controls.

RESULTS AND DISCUSSION

The fabrication of the INCE was characterized by SEM and EDS. As shown in Figure 1 for SEM images, before the sputtering of gold, the bare AAO chip exhibited dense nanochannels with average pore size of ca. 300 nm (Figure 1A), which had minor change after the sputtering of gold (Figure 1B). The cross-sectional view with the gold layer is shown in Figure 1C, which displays the cover of the gold layer on the AAO chip and some gold nanoparticles in the interior of the nanochannel that is close to the outer surface. This might be due to gold atoms entering into the nanochannel during sputtering.[25,42−44] The above results indicate that the sputtering of gold did not block the nanochannel and even had a minor change on the geometry morphology of the AAO nanochannel. As shown in Figure 2 for the EDS image, the gold content on the surface of the the AAO-Au nanochannel after gold deposition increased from 0% to 8% compared to the pristine AAO nanochannel, confirming the presence of Au on the AAO-Au nanochannel. After the assembly of the INCE, the resistance between the wire and its connected side of the INCE chip was less than 200 Ω, while that between the two sides of the INCE chip was not detectable when using a AVO meter with a measure limit of 20 MΩ. The above results demonstrate the high conductivity of the gold layer on the AAO chip and the electrical disconnection of the two sides of the gold layers. Therefore, this new type of INCE should be promising to evolve to a two-electrode system for detection. Generally, there are plenty of reports based on the detection of ion currents using solid-state nanochannels and two-electrode

DOI: 10.1021/acs.analchem.9b03644
Anal. Chem. 2020, 92, 1818−1825

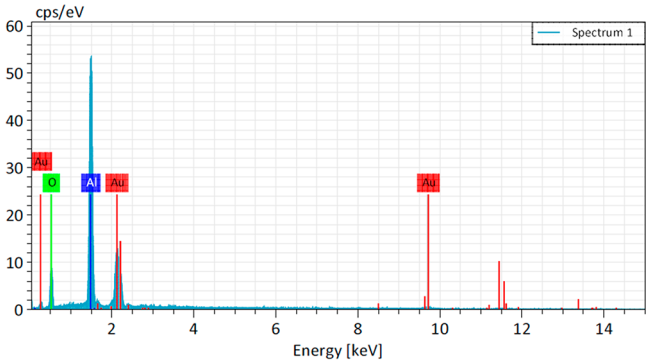

Figure 2. EDS of the outer surface of the INCE.

systems.[11,12,23,45] However, in those systems, electrodes and AAO chips are individual parts, making the volume of the electrolyte cell large and the operation inconvenient, which is clearly not suitable for microminiaturization. Moreover, Ag/AgCl reference electrodes are generally adopted, which is powerful to collect ion currents but hardly feasible for faradic currents, significantly restricting the potential to use other electrochemical methods. Therefore, comparing with conventional nanochannel-electrode systems, the proposed INCE with integrated electrodes and AAO is easy for microminiaturization, convenient for operation, and, more importantly, adoptable for much more electrochemical methods, which should make the INCE an alternative platform to explore more beyond conventional nanochannel systems.

The electrochemical activity of the INCE was evaluated. CV and EIS, as classic electrochemical methods for electrode evaluation, were adopted. A typical three-electrode system was applied, and a commercial Au rod electrode was used for comparison. As shown in Figure 3A for CV curves, both the

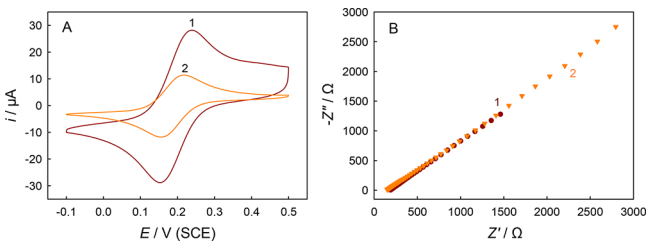

Figure 3. CV (A) and EIS (B) curves of commercial gold rod electrode (1) and INCE (2) in 10 mM $K_3[Fe(CN)_6]/K_4[Fe(CN)_6]$ solution.

INCE and commercial gold electrode presented characteristic redox peaks of the electrochemical probe of $K_3[Fe(CN)_6]/K_4[Fe(CN)_6]$. However, the peak-to-peak potential for the INCE (62 mV) was much less than that for the commercial gold electrode (85 mV), though the latter has indicated a very clean electrode surface.[37] The difference should be ascribed to the higher electrochemical activity of the INCE with nanoporous structure compared with the conventional planar electrode. Imaginably, this merit of the INCE is beneficial to electrochemical detection, since plenty of reports have illustrated much superior performance by using nanoporous electrodes.[46,47] From Figure 3B, EIS showed that the R_{ct} for the INCE was about 0 Ω the same as the commercial gold electrode, both indicating the high electrochemical activity again. In addition, the CV curves of repeated scans on the INCE were almost coincident (not shown), proving the INCE possessed high operation stability. According to the above results, the high electrochemical activity and stability should make the INCE competent as electrochemical platform for further applications.

As the proposed separation-detection system strongly relies on the filtering of MNP-Ab through the nanochannel, the size and the dispersion status of MNP-Ab and the appropriate blocking of the INCE to avoid physical adsorption, are thus crucial. First, the size and the dispersion status of MNP-Ab were characterized by TEM and DLS. Pristine MNPs were set as control. As shown in Figure 4, both MNPs and MNP-Ab

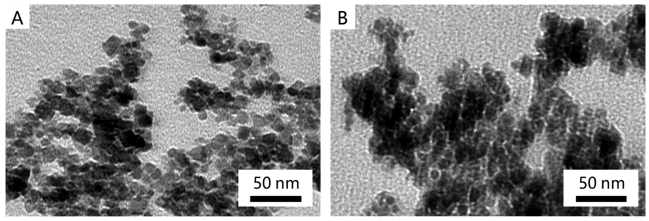

Figure 4. TEM images of MNPs (A) and MNP-Ab (B).

presented as spherical particles with diameter of 15 nm. Note that the modification of a single layer of protein (Ab and BSA) is not distinguishable in TEM images.[48] In addition, DLS measurements gave the hydrodynamic diameters of MNPs and MNP-Ab in aqueous solution, which revealed the actual dispersion status in solution.[49,50] Figure 5 shows the size

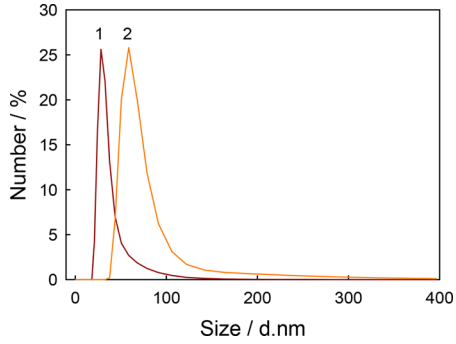

Figure 5. DLS curves of MNPs (1) and MNP-Ab (2).

distribution by number for MNPs and MNP-Ab, which gave an average hydrodynamic diameter of 35 and 71 nm, respectively. Since DLS reflected hydrodynamic diameter not actual size, the size of MNPs measured by DLS was slightly larger than that of TEM.[51] Meanwhile, DLS data clearly indicated an apparent increment in size from MNPs to MNP-Ab, which indicated that MNPs succeeded in conjugation with antibody.[52] As shown in Figure 1B, the actual pore size of AAO-Au nanochannel was ca. 300 nm, with little difference to that provided by the supplier (500 nm), which is four times of the hydrodynamic diameter of MNP-Ab. The large difference between sizes should guarantee size-dependent filtration.

Furthermore, considering the MNP-Ab was blocked using BSA, BSA was thus selected and modified to the INCE to block physical adsorption sites. This procedure was to avoid possible interception of MNP-Ab that interferes seriously with the detection. To investigate the influence of BSA on the adsorption of MNP-Ab, SEM was adopted to characterize the INCE without BSA modification after MNP-Ab filtration. As

DOI: 10.1021/acs.analchem.9b03644
Anal. Chem. 2020, 92, 1818−1825

shown in Figure 6 (A and B), plenty of MNP-Ab were observed on the surface and cross-section of INCE without

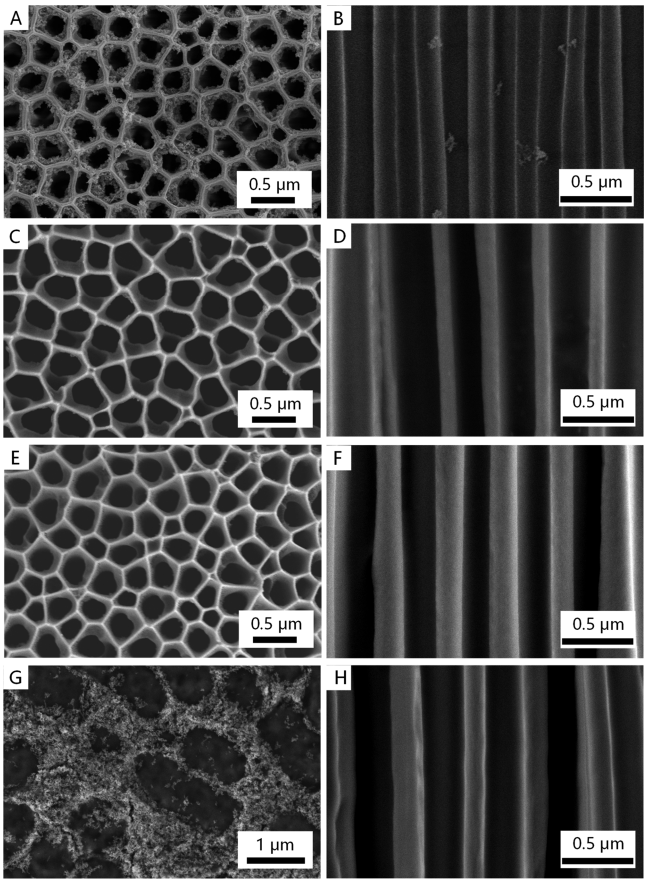

Figure 6. SEM images of the outer surface and corresponding cross-section of INCE after the filtration of MNP-Ab (A, B), INCE-BSA (C, D), INCE-BSA after the filtration of MNP-Ab (E, F), and MNP-Ab-*St* (G, H).

BSA modification, especially on the surface, which would seriously interfere with the surface properties of the nanochannel and further negatively impact on the detection. SEM, CV, and EIS were introduced to characterize the BSA modified INCE (INCE-BSA). Compared to the original INCE, the surface of INCE-BSA showed a few particle-aggregates as observed in the SEM image in Figure 6 (C and D), which was speculated to be BSA due to the low electrical conductivity of BSA.[53] The corresponding cross-sectional image of the nanochannel of the INCE-BSA also displayed an unobstructed channel of ca. 300 nm in diameter, indicating the modification of BSA did not block the nanochannel.

CV and EIS of the INCE-BSA were further collected. Deriving from the integration merit of the INCE, a two-electrode mode was applicable to reflect both the surface properties of the outer surface and the inner nanochannel of INCE. The dropping of two droplets (10 μL) of PBS containing $K_3[Fe(CN)_6]/K_4[Fe(CN)_6]$ onto both sides of INCE was needed to complete the construction of the electrochemical cell system, since liquid rapidly filled in the nanochannel upon the strong capillary force.[54,55] No additional physical electrochemical cell device and reference electrodes (such as Ag/AgCl electrode) were required. This should significantly facilitate the design and operation of the INCE.

As shown in Figure 7A, typical CV curves were obtained before and after BSA modification. A pair of redox peaks

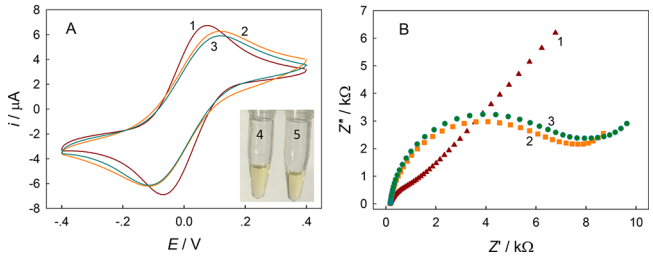

Figure 7. CV (A) and EIS (B) curves of INCE (1), INCE-BSA (2), INCE-BSA with MNP-Ab filtration (3) in 10 mM $K_3[Fe(CN)_6]/K_4[Fe(CN)_6]$ solution. The inset shows the digital picture of the MNP-Ab suspensions before (4) and after (5) filtration.

appeared symmetrically on 0 V. INCE-BSA presented the oxidation peak current of 5.1 ± 0.1 μA and the peak-to-peak potential of 225 ± 5 mV, while those for the INCE were 6.9 ± 0.1 μA and 155 ± 4 mV, respectively. In Figure 7B, EIS curves displayed that R_{ct} increased from 300 ± 30 Ω to 7050 ± 600 Ω after the modification of BSA. The above results clearly demonstrated the successful modification of BSA, which suppressed the electron transfer on the electrode due to its insulativity.

As mentioned above, the successful filtration of MNP-Ab through INCE plays the key pivotal role for the separation and detection. To examine this, CV, EIS, SEM, and digital imaging were used to investigate the surface of the INCE and its nanochannel, as well as the suspension before and after filtration. Figure 7 gives the CV and EIS (curves 3) of INCE-BSA after the filtration of MNP-Ab. The redox peak current slightly decreased compared with that before the filtration, while both the peak-to-peak potential almost remained constant (225 mV) and R_{ct} increased slightly from 7050 ± 600 Ω to 7200 ± 610 Ω, all indicating the surface properties of the INCE had minor change after the filtration. The inset of Figure 7A displays suspensions of MNP-Ab before and after filtration. The color and transparency of both suspensions present undistinguishable change. As shown in Figure 6E, the surface of INCE remained smooth except a few residual MNP-Ab. This might be due to the avoidable interception of MNP-Ab in some concaves. While the interior nanochannels were still smooth without residual MNP-Ab observed (Figure 6F). Therefore, based on the above results, the successful filtration of MNP-Ab should be proved, which was in accordance with our hypothesis and beneficial to further detection of bacteria. The appropriate difference of sizes between MNP-Ab and nanochannel and the blocking of INCE should contribute to this result.

Bacteria with different concentrations were captured by MNP-Ab and then detected using the INCE. The surface and nanochannel were monitored by SEM and EIS. As shown in Figure 6 (G and H), SEM images show the surface and nanochannel of INCE after the filtration, taking the concentration of 10^6 CFU mL^{-1} as an example. Being strongly contrasted to the smooth surface after the filtration of MNP-Ab, plenty of complexes of bacteria and nanoparticles were found. The rod-shaped spots, with width of ca. 0.8 μm and length of 1 μm−2 μm, were *St*.[56,57] In addition to *St*, there were also plenty of MNP-Ab presented and they blocked the electrode surface. These MNP-Ab might be those conjugated

DOI: 10.1021/acs.analchem.9b03644
Anal. Chem. 2020, 92, 1818−1825

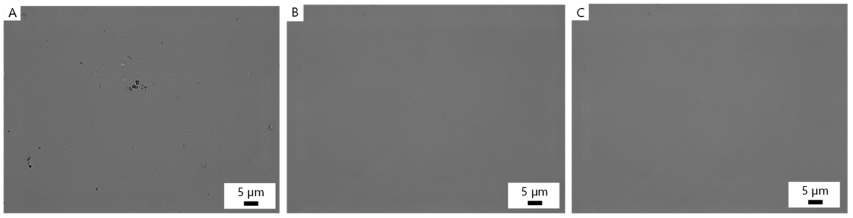

Figure 8. Photos from microscope of the suspension of MNP-Ab-*St* before (A) and after (B) the filtration and the detection solution ($K_3[Fe(CN)_6]/K_4[Fe(CN)_6]$) of the INCE with MNP-Ab-*St* filtration (C).

around *St* and aggregated induced by the bacteria (such as the detached pilus).[56,58] Anyway, the intercepted bacteria and aggregated MNP-Ab caused by the presence of bacteria should cooperatively contribute to the blocking of the surface. No bacteria and MNPs were found in the inner wall surface of nanochannel, as shown in the cross-sectional view in Figure 6H. *St* with much larger size than the pore could not enter into the nanochannel, while free MNP-Ab were easily washed off from nanochannel, as proven above. Moreover, the absence of bacteria in the filtration solution and the detection solution ($K_3[Fe(CN)_6]/K_4[Fe(CN)_6]$) was proven by microscopy imaging. First, the mixtures of MNP-Ab and MNP-Ab-*St* microscope were inspected using microscopy before and after the filtration. As shown in Figure 8A, rod-like *St* was clearly observed in the suspension of MNP-Ab-*St* before the filtration. In contrast, no bacterium was found in the sample after the filtration (Figure 8B). Furthermore, the detection solution ($K_3[Fe(CN)_6]/K_4[Fe(CN)_6]$) was collected and then inspected. As shown in Figure 8C, no bacterium was found, too. Together with the result of SEM image which shows no bacterium in the nanochannel (Figure 6H), it thus can be concluded that the bacteria were absorbed on the surface of INCE without filtrating through the nanochannel or detaching from the INCE.

Figure 9 shows the EIS responses of the INCE to *St* with concentrations from 10^2 to 10^7 CFU mL^{-1}. Along with the

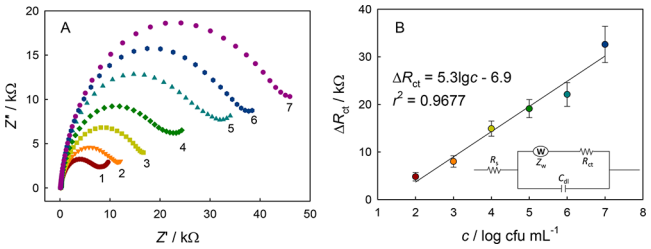

Figure 9. EIS curves (A) of the biosensors responding to MNP-Ab (1) and *St* with concentration ranging from 10^2 to 10^7CFU mL^{-1} (2–7) in 10 mM $K_3[Fe(CN)_6]/K_4[Fe(CN)_6]$ solution. (B) Calibration curve. The inset shows the equivalent circuit. Error bars represent the standard deviation of three independent replicates.

increase of the concentration, the diameter of the semicircles of EIS curves gradually increased, indicating more nanochannels of the INCE were blocked. By using a classic equivalent circuit for the two-electrode system (the inset of Figure 9B),[59] R_{ct} could be simulated and calculated. The difference of R_{ct} to the control (MNP-Ab) (ΔR_{ct}) was thus adopted as the response signal for quantification. As shown in Figure 9B, the ΔR_{ct} presented linear detection range (LDR) from 10^2 to 10^7CFU mL^{-1} (r^2 = 0.9677). The limit of detection (LOD) was calculated to be 50 CFU mL^{-1} (S/N = 3). Although no additional signal labels or signal amplification procedures were applied in this method, the limit of detection is better than or comparable to other analogues (Table 1). The high electro-

Table 1. Summary of Analytical Performance of *St* Detection by Different Methods

Method	LOD (CFU mL^{-1})	LDR (CFU mL^{-1})	Assay time	ref
Thermal sensor	300	300–10^3	1.5 h	58
Paper-based analytical device	10^2	10^3–10^5	75 min	64
Lateral flow immunoassay.	3.5×10^3	1.88×10^4–1.88×10^7	35 min	57
Optical biosensor	10	10^5–10^7	>1 h	56
Electrochemical biosensor	10	10^1–10^6	125 min	65
Microfluidic biosensor	33	3.7×10^1–3.7×10^6	2 h	66
Separation-detection system based on INCE	50	10^2–10^7	<1 h	this work

chemical activity of the nanoporous surface of the INCE, the high sensitivity of electrochemistry on surficial properties, and the ability of the INCE for thorough filtration of MNP-Ab, should cooperatively contribute to the satisfactory detection performance. Moreover, the time required to obtain the final signal from the sample was less than 1 h; Only procedures of incubation, magnetic separation, filtration in INCE, and EIS signal readout are needed for whole detection, which are quite facile compared with analogues with much more and complicated procedures, such as repeated magnetic separation, conjugation of signal labels, and signal amplification. Clearly, the simplified procedures are beneficial for time-efficiency and reproducibility.

Furthermore, the specificity of this biosensor was investigated by comparing the EIS responses of the target bacteria (*St*) to the four different interfering bacteria. These four common foodborne bacteria are rod-shaped, including *Ec* (ca. 0.5 μm × 2 μm),[27] *Vp* (0.5–0.8 μm × 1.4–2.6 μm),[60] *Lm* (ca. 1 μm × 2–5 μm),[61] and globular-shaped bacteria, *Sa* (ca. 1 μm).[62,63] Similar to *St*, they were separately incubated with MNP-Ab (Anti-*St*), and each sample was filtered and measured on the INCE individually. As shown in Figure 10, the response of the biosensor to all four types of interfering bacteria with the concentration of 1×10^4 CFU mL^{-1} was less than 13% of that of *St* with the same concentration. This should prove the satisfactory specificity and potential for real sample application.

CONCLUSIONS

We have successfully developed a cooperation mode of the outer surface and inner space of nanochannel based on the

DOI: 10.1021/acs.analchem.9b03644
Anal. Chem. 2020, 92, 1818–1825

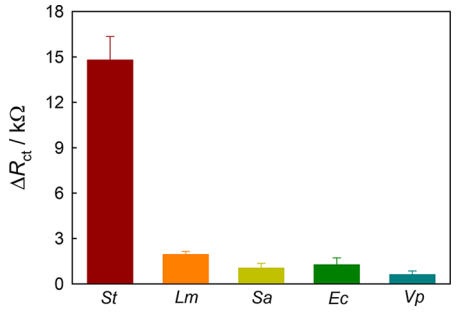

Figure 10. EIS responses of the biosensor to different bacteria with identical concentration of 1×10^4 CFU mL^{-1}. Error bars represent the standard deviation of three independent replicates.

INCE and its application for separation−detection system to detect bacteria in a rapid and facile way. The INCE explored the outer surface of nanochannel as highly sensitive interface and the nanochannel as highly efficient nanofilter, showing significant potential to facilely separate nanoparticles via the size variety and sensitively probe the presence of intercepted entities. Due to the integration effect, the INCE evolved a unique two-electrode mode with both Au layers as electrodes and the nanochannel as the electrochemical cell, which brought convenience for operation and great potential for microminiaturization in addition to the inherent high electrochemical sensitivity. Therefore, together with the utilization of MNPs, the separation−detection system has been readily elaborated to develop a novel biosensing strategy eliminating the requirement of additional signal labels. The biosensor presented a LDR between the concentrations ranging from 10^2 to 10^7 CFU mL^{-1} and a LOD of 50 CFU mL^{-1}, being comparable or even better than those of analogues with complicated signal amplification designs. Moreover, this biosensing method avoided the requirement on specially designed electrochemical cell and large-volume solution, which made it rapid and facile in operation. This study extends the research to the outer surface of nanochannel and may inspire a series of new thoughts. The separation−detection system also provides a promising platform for the detection of targets with varied size to the pore size separation, which is especially useful to the detection of bacteria and virus in clinic diagnosis, food safety, and environmental monitoring.

AUTHOR INFORMATION

Corresponding Author

*E-mail: ycfu@zju.edu.cn.

ORCID

Yibin Ying: 0000-0002-3392-9380

Yingchun Fu: 0000-0003-0550-9052

Notes

The authors declare no competing financial interest.

ACKNOWLEDGMENTS

This research was supported by the National Natural Science Foundation of China (Grant 21775137).

REFERENCES

(1) Dekker, C. *Nat. Nanotechnol.* **2007**, *2*, 209−215.
(2) Long, Z.; Zhan, S. S.; Gao, P. C.; Wang, Y. Q.; Lou, X. D.; Xia, F. *Anal. Chem.* **2018**, *90*, 577−588.
(3) Karan, S.; Samitsu, S.; Peng, X. S.; Kurashima, K.; Ichinose, I. *Science* **2012**, *335*, 444−447.
(4) Karan, S.; Jiang, Z. W.; Livingston, A. G. *Science* **2015**, *348*, 1347−1351.
(5) Liu, Y. P.; Shen, D. K.; Chen, G.; Elzatahry, A. A.; Pal, M.; Zhu, H. W.; Wu, L. L.; Lin, J. J.; Al-Dahyan, D.; Li, W.; Zhao, D. Y. *Adv. Mater.* **2017**, *29*, 1702274.
(6) Siria, A.; Poncharal, P.; Biance, A. L.; Fulcrand, R.; Blase, X.; Purcell, S. T.; Bocquet, L. *Nature* **2013**, *494*, 455−458.
(7) Gao, J.; Guo, W.; Feng, D.; Wang, H. T.; Zhao, D. Y.; Jiang, L. *J. Am. Chem. Soc.* **2014**, *136*, 12265−12272.
(8) Long, R.; Kuang, Z. F.; Liu, Z. C.; Liu, W. *Phys. Chem. Chem. Phys.* **2018**, *20*, 7295−7302.
(9) Sui, X.; Zhang, Z.; Li, C.; Gao, L. C.; Zhao, Y.; Yang, L. J.; Wen, L. P.; Jiang, L. *ACS Appl. Mater. Interfaces* **2019**, *11*, 23815−23821.
(10) Wongkaew, N.; Simsek, M.; Griesche, C.; Baeumner, A. J. *Chem. Rev.* **2019**, *119*, 120−194.
(11) Zhang, R.; Chen, X.; Sun, Z.; Chen, S.; Gao, J.; Sun, Y.; Li, H. *Anal. Chem.* **2019**, *91*, 6149−6154.
(12) Wang, J.; Hou, J.; Zhang, H. C.; Tian, Y.; Jiang, L. *ACS Appl. Mater. Interfaces* **2018**, *10*, 2033−2039.
(13) Reta, N.; Michelmore, A.; Saint, C. P.; Prieto-Simon, B.; Voelcker, N. H. *ACS Sens.* **2019**, *4*, 1515−1523.
(14) Guo, K. Y.; Sharma, A.; Toh, R. J.; de Eulate, E. A.; Gengenbach, T. R.; Ceto, X.; Voelcker, N. H.; Prieto-Simon, B. *Adv. Funct. Mater.* **2019**, *29*, 1809206
(15) Reta, N.; Michelmore, A.; Saint, C.; Prieto-Simon, B.; Voelcker, N. H. *Biosens. Bioelectron.* **2016**, *80*, 47−53.
(16) Brodoceanu, D.; Elnathan, R.; Prieto-Simon, B.; Delalat, B.; Guinan, T.; Kroner, E.; Voelcker, N. H.; Kraus, T. *ACS Appl. Mater. Interfaces* **2015**, *7*, 1160−1169.
(17) Hou, X.; Zhang, H. C.; Jiang, L. *Angew. Chem., Int. Ed.* **2012**, *51*, 5296−5307.
(18) Ai, M.; Ahmed, I.; Nasir, S.; Ramirez, P.; Niemeyer, C. M.; Mafe, S.; Ensinger, W. *ACS Appl. Mater. Interfaces* **2015**, *7*, 19541−19545.
(19) Meng, Z. Y.; Chen, Y.; Li, X. L.; Xu, Y. L.; Zhai, J. *ACS Appl. Mater. Interfaces* **2015**, *7*, 7709−7716.
(20) Zhang, H. C.; Tian, Y.; Jiang, L. *Nano Today* **2016**, *11*, 61−81.
(21) Guo, W.; Hong, F.; Liu, N. N.; Huang, J. Y.; Wang, B. Y.; Duan, R. X.; Lou, X. D.; Xia, F. *Adv. Mater.* **2015**, *27*, 2090−2095.
(22) Wang, H. M.; Hou, S. N.; Wang, Q. Q.; Wang, Z. W.; Fan, X.; Zhai, J. *J. Mater. Chem. B* **2015**, *3*, 1699−1705.
(23) Niu, B.; Xiao, K.; Huang, X. D.; Zhang, Z.; Kong, X. Y.; Wang, Z. Q.; Wen, L. P.; Jiang, L. *ACS Appl. Mater. Interfaces* **2018**, *10*, 22632−22639.
(24) Sun, Y.; Chen, S.; Chen, X. Y.; Xu, Y. L.; Zhang, S. Y.; Ouyang, Q. Y.; Yang, G. F.; Li, H. B. *Nat. Commun.* **2019**, *10*, 1323.
(25) Gao, P. C.; Ma, Q.; Ding, D. F.; Wang, D. G.; Lou, X. D.; Zhai, T. Y.; Xia, F. *Nat. Commun.* **2018**, *9*, 4557.
(26) Li, X. C.; Zhai, T. Y.; Gao, P. C.; Cheng, H. L.; Hou, R. Z.; Lou, X. D.; Xia, F. *Nat. Commun.* **2018**, *9*, 40.
(27) Chan, K. Y.; Ye, W. W.; Zhang, Y.; Xiao, L. D.; Leung, P. H. M.; Li, Y.; Yang, M. *Biosens. Bioelectron.* **2013**, *41*, 532−537.
(28) Frey, N. A.; Peng, S.; Cheng, K.; Sun, S. H. *Chem. Soc. Rev.* **2009**, *38*, 2532−2542.
(29) Lee, I. S.; Lee, N.; Park, J.; Kim, B. H.; Yi, Y. W.; Kim, T.; Kim, T. K.; Lee, I. H.; Paik, S. R.; Hyeon, T. *J. Am. Chem. Soc.* **2006**, *128*, 10658−10659.
(30) Mornet, S.; Vasseur, S.; Grasset, F.; Duguet, E. *J. Mater. Chem.* **2004**, *14*, 2161−2175.
(31) Weissleder, R.; Kelly, K.; Sun, E. Y.; Shtatland, T.; Josephson, L. *Nat. Biotechnol.* **2005**, *23*, 1418−1423.
(32) Lan, L. Y.; Yao, Y.; Ping, J. F.; Ying, Y. B. *Biosens. Bioelectron.* **2017**, *91*, 504−514.
(33) Reddy, L. H.; Arias, J. L.; Nicolas, J.; Couvreur, P. *Chem. Rev.* **2012**, *112*, 5818−5878.
(34) Lim, M. C.; Kim, Y. R. *J. Microbiol. Biotechnol.* **2016**, *26*, 1505−1516.

DOI: 10.1021/acs.analchem.9b03644
Anal. Chem. 2020, 92, 1818−1825

(35) Sun, Y.; Fang, L. Y.; Wan, Y.; Gu, Z. F. *Sens. Actuators, B* **2018**, *259*, 428−432.
(36) Wang, Y.; Alocilja, E. C. *J. Biol. Eng.* **2015**, *9*, 16.
(37) Cao, L. L.; Zhang, Q.; Dai, H.; Fu, Y. C.; Li, Y. B. *Electroanalysis* **2018**, *30*, 517−524.
(38) Wang, J. H.; Morton, M. J.; Elliott, C. T.; Karoonuthaisiri, N.; Segatori, L.; Biswal, S. L. *Anal. Chem.* **2014**, *86*, 1671−1678.
(39) Yang, L. J.; Ruan, C. M.; Li, Y. B. *Biosens. Bioelectron.* **2003**, *19*, 495−502.
(40) Lin, J. H.; Li, M.; Li, Y. B.; Chen, Q. *J. Magn. Magn. Mater.* **2015**, *378*, 206−213.
(41) Zheng, L. Y.; Cai, G. Z.; Wang, S. Y.; Liao, M.; Li, Y. B.; Lin, J. H. *Biosens. Bioelectron.* **2019**, *124*, 143−149.
(42) Shi, L.; Mu, C. L.; Gao, T.; Chai, W. X.; Sheng, A. Z.; Chen, T. S.; Yang, J.; Zhu, X. L.; Li, G. X. *J. Am. Chem. Soc.* **2019**, *141*, 8239−8243.
(43) Zhao, X. P.; Zhou, Y.; Zhang, Q. W.; Yang, D. R.; Wang, C.; Xia, X. H. *Anal. Chem.* **2019**, *91*, 1185−1193.
(44) Cao, J.; Zhao, X. P.; Younis, M. R.; Li, Z. Q.; Xia, X. H.; Wang, C. *Anal. Chem.* **2017**, *89*, 10957−10964.
(45) Lu, Q.; Tang, Q. H.; Chen, Z. H.; Zhao, S. L.; Qing, G. Y.; Sun, T. L. *ACS Appl. Mater. Interfaces* **2017**, *9*, 32554−32564.
(46) Xi, F. N.; Xuan, L. L.; Lu, L. L.; Huang, J.; Yan, F.; Liu, J. Y.; Dong, X. P.; Chen, P. *Sens. Actuators, B* **2019**, *288*, 133−140.
(47) Cheng, B. W.; Zhou, L.; Lu, L. L.; Liu, J. Y.; Dong, X. P.; Xi, F. N.; Chen, P. *Sens. Actuators, B* **2018**, *259*, 364−371.
(48) Fu, K. Y.; Zheng, Y.; Li, J.; Liu, Y. S.; Pang, B.; Song, X. L.; Xu, K.; Wang, J.; Zhao, C. *J. Agric. Food Chem.* **2018**, *66*, 9516−9521.
(49) de la Torre, T. Z. G.; Stromberg, M.; Russell, C.; Goransson, J.; Nilsson, M.; Svedlindh, P.; Stromme, M. *J. Phys. Chem. B* **2010**, *114*, 3707−3713.
(50) Tiwari, A. P.; Satvekar, R. K.; Rohiwal, S. S.; Karande, V. A.; Raut, A. V.; Patil, P. G.; Shete, P. B.; Ghosh, S. J.; Pawar, S. H. *RSC Adv.* **2015**, *5*, 8463−8470.
(51) Lim, J.; Yeap, S. P.; Che, H. X.; Low, S. C. *Nanoscale Res. Lett.* **2013**, *8*, 381.
(52) Liu, X.; Dai, Q.; Austin, L.; Coutts, J.; Knowles, G.; Zou, J. H.; Chen, H.; Huo, Q. *J. Am. Chem. Soc.* **2008**, *130*, 2780−2782.
(53) Mikhaylova, M.; Kim, D. K.; Berry, C. C.; Zagorodni, A.; Toprak, M.; Curtis, A. S. G.; Muhammed, M. *Chem. Mater.* **2004**, *16*, 2344−2354.
(54) Sparreboom, W.; van den Berg, A.; Eijkel, J. C. T. *Nat. Nanotechnol.* **2009**, *4*, 713−720.
(55) Li, L. X.; Kazoe, Y.; Mawatari, K.; Sugii, Y.; Kitamori, T. *J. Phys. Chem. Lett.* **2012**, *3*, 2447−2452.
(56) Wen, C. Y.; Hu, J.; Zhang, Z. L.; Tian, Z. Q.; Ou, G. P.; Liao, Y. L.; Li, Y.; Xie, M.; Sun, Z. Y.; Pang, D. W. *Anal. Chem.* **2013**, *85*, 1223−1230.
(57) Hu, J.; Jiang, Y. Z.; Tang, M.; Wu, L. L.; Xie, H. Y.; Zhang, Z. L.; Pang, D. W. *Anal. Chem.* **2019**, *91*, 1178−1184.
(58) Zhang, Z.; Wang, Q.; Han, L. Y.; Du, S. Y.; Yu, H. F.; Zhang, H. Y. *Sens. Actuators, B* **2018**, *268*, 188−194.
(59) Joung, C. K.; Kim, H. N.; Lim, M. C.; Jeon, T. J.; Kim, H. Y.; Kim, Y. R. *Biosens. Bioelectron.* **2013**, *44*, 210−215.
(60) Bisha, B.; Simonson, J.; Janes, M.; Bauman, K.; Goodridge, L. D. *Int. J. Food Sci. Technol.* **2012**, *47*, 885−899.
(61) Lv, E. G.; Ding, J. W.; Qin, W. *Anal. Chem.* **2018**, *90*, 13600−13606.
(62) Ryan, S.; Kell, A. J.; van Faassen, H.; Tay, L. L.; Simard, B.; MacKenzie, R.; Gilbert, M.; Tanha, J. *Bioconjugate Chem.* **2009**, *20*, 1966−1974.
(63) Liao, X. W.; Yang, F.; Li, H. Y.; So, P. K.; Yao, Z. P.; Xia, W.; Sun, H. Z. *Inorg. Chem.* **2017**, *56*, 14823−14830.
(64) Srisa-Art, M.; Boehle, K. E.; Geiss, B. J.; Henry, C. S. *Anal. Chem.* **2018**, *90*, 1035−1043.
(65) Melo, A. M. A.; Alexandre, D. L.; Oliveira, M. R. F.; Furtado, R. F.; Borges, M. F.; Ribeiro, P. R. V.; Biswas, A.; Cheng, H. N.; Alves, C. R.; Figueiredo, E. A. T. *J. Solid State Electrochem.* **2018**, *22*, 1321−1330.
(66) Hou, Y.; Cai, G. Z.; Zheng, L. Y.; Lin, J. H. *Food Control* **2019**, *103*, 186−193.

DOI: 10.1021/acs.analchem.9b03644
Anal. Chem. 2020, 92, 1818−1825